

Tetrahedrites Synthesized via Scalable Mechanochemical Process and Spark Plasma Sintering

Peter Baláž,¹ Emanuel Guilmeau,^{2,*} Nina Daneu,³ Oleksandr Dobrozhan,^{4,*} Matej Baláž,¹ Michal Hegedus,⁵ Tristan Barbier,² Marcela Achimovičová,¹ Mária Kaňuchová,⁶ Jaroslav Briančin¹

¹ Institute of Geotechnics, Slovak Academy of Sciences, 04353 Košice, Slovakia

² CRISMAT, CNRS, Normandie University, ENSICAEN, UNICAEN, 14000 Caen, France

³ Jozef Stefan Institute, S1-1000 Ljubljana, Slovenia

⁴ Sumy State University, 40007 Sumy, Ukraine

⁵ Synthon,s.r.o., 67801 Blansko, Czech Republic

⁶ Institute of Earth Resources, Technical University Košice, 04001 Košice, Slovakia

Corresponding authors: emmanuel.guilmeau@ensicaen.fr, o.dobrozhan@ekt.sumdu.edu.ua

ABSTRACT

In this study, we demonstrate the use of elemental precursors (Cu,Sb,S) to synthesize tetrahedrite $\text{Cu}_{12}\text{Sb}_4\text{S}_{13}$ using an industrial eccentric vibratory mill. Mechanochemical synthesis of tetrahedrite leads to the formation of covellite (CuS), skinnerite (Cu_3SbS_3) or famatinite (Cu_3SbS_4) in dependence on milling time. However, the composite product can be modified in favour of prevailing tetrahedrite when Spark Plasma Sintering (SPS) treatment is applied after milling. The as-synthesized and sintered products are composed of polydisperse nanosized particles with dimensions up to 250 nm. The thermoelectric measurements reveal a maximum value of figure-of-merit $ZT = 0.67 @ 700\text{K}$, as a consequence of a relatively high power factor ($1.07 \text{ mW m}^{-1} \text{ K}^{-2}$) and a low thermal conductivity ($1.12 \text{ W m}^{-1} \text{ K}^{-1}$). The obtained ZT values for products prepared in an industrial mill are comparable to the ones synthesized by milling in

laboratory mills. The synthesis of ternary and quaternary sulphides by a scalable and industrializable milling process represents a prospective route for mass production of thermoelectric materials.

1. INTRODUCTION

Tetrahedrites represent the most important source of copper and antimony and are also economically attractive due to their content of silver and mercury [1]. Extractive metallurgy has been applied to selectively obtain copper and precious metals from these minerals. Several technologies have been developed like SUNSHINE in the USA and MELT in Slovakia [2]. However, their start-ups have been problematic as a consequence of a decline in mining and metallurgy of primary sulfidic ores.

Less than two decades were needed for tetrahedrite to be back on stage. In 2012, Suekuni *et al.* [3] highlighted thermoelectric performance in a synthetic tetrahedrite and a new era for applications of ternary and quaternary sulphides as prospective energy materials, with tetrahedrite as a flagship has started.

Tetrahedrites form a large group of naturally-occurring sulfosalts of composition $X_{10}Y_2Z_4Q_{13}$ where $X = \text{Cu, Ag}$; $Y = \text{Cu, Mn, Fe, Co, Ni, Zn, Hg, Cd}$; $Z = \text{Sb, As, Bi}$; $Q = \text{S, Se, Te}$ [4]. According to this formula, ten copper atoms are in the +1 oxidation state and the remaining two copper atoms are in the +2 oxidation state. Copper can be substituted by various transition metals [5, 6]. Antimony is in +3 oxidation state and sulphur is in -2 oxidation state [7, 8]. The tetrahedrite phase has a body-centred cubic ($I\bar{4}3m$) complex crystal structure which contains 58 atoms on 5 distinct crystallographic sites [3]. This structure consists of three units formed by Cu in planar triangular coordination and tetrahedral coordination, and SbS_3 in trigonal pyramid where Sb is coordinated by three S [9, 10].

Thermoelectric power and electrical resistivity of natural tetrahedrite minerals have been reported already in the 50th [11]. However, only when ultra-low thermal conductivity of tetrahedrite has been evidenced [3], the number of papers on this topic dramatically increased. Several PhD studies were initiated [12-16] and several review papers were published recently [7-8, 17-19]. The complex crystal structure of tetrahedrite focused the understanding of the low thermal conductivity into inspecting its bonding variability. Here, copper in planar coordination between three sulphur atoms, co-operating with the lone pairs of the two antimony atoms, is characterized by large out-of-plane rattling modes, which play a decisive role in the scattering of acoustic phonons [19-22].

There are several ways to improve the performance of thermoelectric materials. Besides the search for efficient thermoelectric materials, doping in the case of tetrahedrite is well documented [3, 7-8, 12-19, 23-39] and the nanostructuring approach plays still more and more important role in the synthesis of thermoelectrics [40-45]. Here the increased phonon scattering, as a consequence of created grain boundaries and structural defects in nanostructures, leads to low thermal conductivity.

Mechanochemistry is an easy, scalable and reproducible method for the production of nanograins [2, 46-54]. Moreover, the mechanochemically synthesized (sometimes called mechanically alloyed) structures are created by a well-crystallized core of nanoparticles with disordered near-surface shell regions [55], which can potentially favour a decrease in the thermal conductivity. Bulk nanostructuring approach via combination of high energy milling with hot pressing methods has been applied for the preparation of plethora nanostructured thermoelectric compounds [44]. This combined method has been developed especially for the preparation of various non-doped tetrahedrites (**Table 1**). In this case, SPS treatment was mainly used for the densification of the nanopowders synthesized by mechanochemistry. More

detailed insight into the thermoelectric properties of non-doped tetrahedrite produced by various synthetic and consolidation methods is given in ESI (**Table S1**).

As the effectiveness of the combination of mechanochemistry and SPS has already been proven at laboratory level, the aim of this work has been focused on the development of industrial milling for the synthesis of tetrahedrite $\text{Cu}_{12}\text{Sb}_4\text{S}_{13}$ followed by SPS. We report in this study ZT values comparable to the ones obtained in laboratory mills (**Table 1**). The relationship between the phase composition, nano-microstructure and transport properties of the final products is discussed in the following.

Table 1. Figure of merit ZT of pristine tetrahedrites $\text{Cu}_{12}\text{Sb}_4\text{S}_{13}$ synthesized via the combination of high energy milling and spark plasma sintering

ZT	T (K)	High energy milling	Reference
0.55	673	Laboratory	[3]
0.56	673	Laboratory	[26]
0.30	623	Laboratory	[33]
0.76	623	Laboratory	[7,8]
0.42	573	Laboratory	[13]
0.65	673	Laboratory	[29]
0.59	673	Laboratory	[14]
0.68	623	Laboratory	[56]
0.86	723	Laboratory	[57]
0.67	700	Industrial	This work

2. MATERIALS AND METHODS

For mechanochemical synthesis of tetrahedrite $\text{Cu}_{12}\text{Sb}_4\text{S}_{13}$, the following elemental precursors were used: copper (Merck, 99% purity, 99% particles below 70 micrometers), antimony (Alpha Aesar, 99.5% purity, 99% particles below 120 micrometers) and sulphur (CG-Chemikalien, 99% purity, 99% particles below 390 micrometers).

Mechanochemical solid-state syntheses were carried out in an industrial eccentric vibratory ball mill ESM 656-0.5 ks (Siebtechnik, Germany) working under the following conditions: 5L steel satellite milling chamber attached to the main corpus of the mill, tungsten carbide balls with a diameter of 35 mm and total mass of 25 kg, 80% ball filling in milling chamber, amplitude of the mill 20 mm, rotational speed of the eccentric 960 min^{-1} , argon atmosphere. The total feed of reaction precursors is 100 grams per batch. The milling was performed at different times, *i.e.* 1-6 h. The photographs of the mill together with the attached satellite chamber are shown in ESI (**Fig. S1**).

After completion of the milling programs, the resulting pulverized powder was shaped and densified using SPS (FCT HPD 25) at 723 K for 30 minutes (heating and cooling rate of 100 K/min) under a pressure of 64 MPa using graphite dies of 10 mm diameter and a slight overpressure of 30 hPa (Ar), in order to prevent both oxidation and sulphur volatilization. The final thickness of the pellets was around 8 mm with a geometrical density in excess of 95 % of the crystallographic value.

The qualitative identification of the phase composition was performed by XRD method with an X'Pert PW 3040 MPD diffractometer (Phillips) working in the 2θ geometry with $\text{CuK}\alpha$ radiation. XRD patterns of sintered samples were collected using a D8 Advance diffractometer (Bruker, Germany) with the $\text{CuK}\alpha$ radiation in the Bragg–Brentano configuration. The generator was set up at 40 kV and 40 mA. The divergence and receiving slits were 0.3° and 0.1 mm, respectively. The XRD patterns were recorded in the range of $10\text{--}80^\circ 2\theta$ with a step of 0.05° . Rietveld refinements of XRD data of the as-prepared solid solutions were performed in the space group $I\bar{4}3m$ using Fullprof software [58]. The XRD line broadening was analyzed by the refinement of regular Thompson–Cox–Hastings pseudo-Voigt function parameters. In order to obtain proper geometry set-up and to eliminate instrumental broadening, the

instrumental resolution function was determined by refinement of the LaB₆ standard specimen. The JCPDS PDF database was utilized for phase identification [59].

The content of non-reacted elemental sulphur in the samples was determined by a simple gravimetric method using a Soxhlet extractor. The extraction thimble was loaded with well-weighed 1 g of powder sample and placed into the main chamber of the extractor. 30 mL of carbon disulphide (99.9%, Fischer Chemical) was placed into a 500 mL distilling flask and the apparatus was set up. Upon heating of the flask in a hot water bath, three cycles were run to quantitatively dissolve all sulphur present in the sample. The resulting solution cooled to room temperature was transferred into a 250 mL round bottom flask of a known mass and the solvent was distilled under vacuum. The flask was further dried at 70 °C to eliminate any traces of the solvent and re-weighed. Conversion degree α of corresponding mechanochemical synthesis was calculated based on Soxhlet analysis according to the formula:

$$\alpha = 100 - ((m_{f1}-m_{f0})/m_{s0}) \quad (1)$$

where α is overall conversion degree, m_{s0} the starting amount of sulphur in the reaction mixture (g), m_{f1} the mass of the flask after extraction (g), and m_{f0} the mass of the flask before extraction (g).

XPS apparatus SPECS with PHOIBOS 100 SCD and non-monochromatic X-ray source was used. The core spectra were measured at 70 eV and the survey spectrum at 70 eV using room temperature. Basic pressure 1.10^{-8} mbar with AlK _{α} excitation at 10 kV for all spectra were acquired. For data analysis, SpecsLab2 CasaXPS software (Casa Software Ltd.) was used. All peaks were fitted with Shirley and Tougaard type baseline. Silver (Ag3d) was used for calibration of the spectrometer. Charging of samples was resolved by the calibration on carbon.

Scanning electron microscopy images were recorded using MIRA 3 FE-SEM microscope (TESCAN Czech Republic) equipped with EDX detector (Oxford Instrument, United Kingdom) or a field-emission gun scanning electron microscope (FEG-SEM; JSM-7600F, Jeol

Ltd., Tokyo, Japan) operated at 10-20 kV and equipped with an energy dispersive X-ray spectrometer (EDS; INCA Oxford 350 EDS SDD, Oxfordshire, UK). EDS analyses were performed at 20 kV and 15 mm working distance. The samples were ground and polished, final polishing was done on 3-microns diamond lapping film. Cross-sections perpendicular and transversal to the applied pressure during SPS sintering were analyzed to check for potential texturization in the sintered samples. For Transmission Electron Microscopy (TEM) analyses, the samples were prepared according to the conventional procedure using thinning, dimpling and ion-milling. The sintered compacts were inserted into a brass tube with 3-mm diameter for support and fixed with epoxy resin. The samples were thinned from both sides to form around 100 microns thin discs, which were further dimpled to around 15-microns in the disc center. Electron-transparent regions were obtained by ion milling (Gatan Pips 691, California, USA) using 3.8 kV Ar⁺ ions at an incidence angle of 10° until perforation. Prior to TEM analyses, the specimens were coated by a thin layer of carbon to improve surface electron conductivity. TEM analyses were performed on a 200-kV probe-aberration corrected atomic-resolution scanning transmission electron microscope (JEOL ARM200 CF, Jeol Ltd., Tokyo, Japan) equipped with energy dispersive x-ray spectrometer (Jeol Centurio 100).

The electrical resistivity (ρ) and Seebeck coefficient (S) were measured simultaneously from ingots, from 300 K up to 700 K using an ULVAC-ZEM3 device under partial helium pressure.

A NETZSCH LFA-457 apparatus was used for measuring the thermal diffusivity under argon flow. The thermal conductivity (κ) was determined as the product of the geometrical density, the thermal diffusivity, and the theoretical heat capacity using the Dulong–Petit approximation.

The Wiedemann-Franz law, using a Lorenz number estimated from the relationship $L = 1.5 + \exp(-|S|/116)$, [60] was used to calculate the lattice thermal conductivity by subtracting the electronic contribution to the total thermal conductivity ($\kappa_L = \kappa - \kappa_e$). The estimated

measurement uncertainties are 6% for the Seebeck coefficient, 8% for the electrical resistivity, 11% for the thermal conductivity, and 16% for the final figure of merit, ZT [61].

3. RESULTS AND DISCUSSION

3.1. Phase formation during mechanochemical synthesis

XRD patterns of stoichiometric mixtures of Cu, Sb and S precursors co-milled in an industrial mill are shown in **Fig. S1**. Milling times of 1-6 hours have been applied. Consecutive formation of binary and ternary sulphides is clearly evidenced (see also **Table 2**), as shown in our previous works on the mechanochemical synthesis of multinary sulphides for solar cells applications [46-47, 62-65]. Strong affinity of copper with sulphur leads to the formation of copper sulphides [66]. In our case, small amounts of CuS and Cu₂S were formed already during mixing precursors to prepare homogeneous input into the mill (**Table 2**).

Table 2. XRD qualitative analysis of mechanochemically synthesized powders (L corresponds to low content of phase).

Milling time (h)	Identified phase								Sample name
	Cu	Sb	S	Cu ₂ S	CuS	Cu ₃ SbS ₃	Cu ₃ SbS ₄	Cu ₁₂ Sb ₄ S ₁₃	
0	+	+	+	+	+				M0
1					+	+	+	+	M1
2					+	+	+	+	M2
3					L	+	+	+	M3
4						L	+	+	M4
6							+	+	M6

Starting from 1 hour of milling, four products of mechanochemical synthesis have been detected, *i.e.* covellite CuS (space group: $P6_3/mmc$), skinnerite Cu₃SbS₃ (space group: $P2_1/c$), famatinitite Cu₃SbS₄ (space group: $I\bar{4}2m$), and tetrahedrite Cu₁₂Sb₄S₁₃ (space group: $I\bar{4}3m$). With increasing milling time, the contents of CuS and Cu₃SbS₃ are decreasing while Cu₃SbS₄ and Cu₁₂Sb₄S₁₃ are the only present phases. Tetrahedrite starts slowly to prevail over famatinitite. However, even after 6 hours of milling, both phases are still the most dominant. Compared to

ball-milling in laboratory where the tetrahedrite phase is almost fully formed after only 5h [25], it seems that the eccentric vibratory ball-milling conditions in our study are less energetic to lead to complete crystallization of the tetrahedrite phase.

In principle, four ternary phases can exist in Cu-Sb-S system: chalkostibnite CuSbS_2 (space group: *Pnam*), skinnerite Cu_3SbS_3 , famatinitite Cu_3SbS_4 , and tetrahedrite $\text{Cu}_{12}\text{Sb}_4\text{S}_{13}$. The corresponding free energy values ΔG are $-138.5 \text{ kJ}\cdot\text{mol}^{-1}$, $-216,9 \text{ kJ}\cdot\text{mol}^{-1}$, $-266.6 \text{ kJ}\cdot\text{mol}^{-1}$ and $-917.2 \text{ kJ}\cdot\text{mol}^{-1}$, respectively [67]. According to these values, the incidence of tetrahedrite and famatinitite phases are the most feasible in solid-state synthesis.

We hypothesize that two parallel reactions proceed during milling. First, the thermodynamically most feasible synthesis of tetrahedrite is realized. Then, the produced nano-grained and reactive tetrahedrite is forced to evolve elemental sulphur which backward reacts with tetrahedrite to form famatinitite. Indeed, the co-existence of famatinitite with tetrahedrite has been evidenced by the study of tetrahedrite stability relations in Cu-Sb-S system [68]. In this case, temperatures of 250-300 °C were sufficient for the formation of famatinitite from partly decomposed tetrahedrite. Evidence of hot spots with temperatures several hundred degrees at contact points of milling balls with milled material has been verified in mechanochemistry many times (see e.g. hot-spot theory in [2]) and can play role also in our case.

In the thermoelectric community, there is a tendency to suppress famatinitite because it reduces the thermoelectric performance of tetrahedrite due to its low electrical conductivity and large thermal conductivity [69, 70]. For this purpose, the seed matrix containing only natural tetrahedrite (50%) together with addition of the elemental precursors was investigated by Morreli's group [12, 26-29]. In this case, famatinitite as a product becomes minute. Famatinitite suppression was also realized by doping of tetrahedrite and/or by SPS post-treatment after milling [26-30, 33, 56, 68, 71]. In our case, XRD patterns of co-milled reaction precursors with subsequent SPS treatment are illustrated in **Fig. 1**. The very good selectivity for the

tetrahedrite/famatinite ratio was obtained only for sample milled for one hour. In this case, the content of tetrahedrite was over 99 wt%, while for samples milled for longer times it approximately oscillates around 80 wt%. This suggests that the famatinite phase stabilized during ball-milling is difficult to transform during subsequent fast SPS treatment.

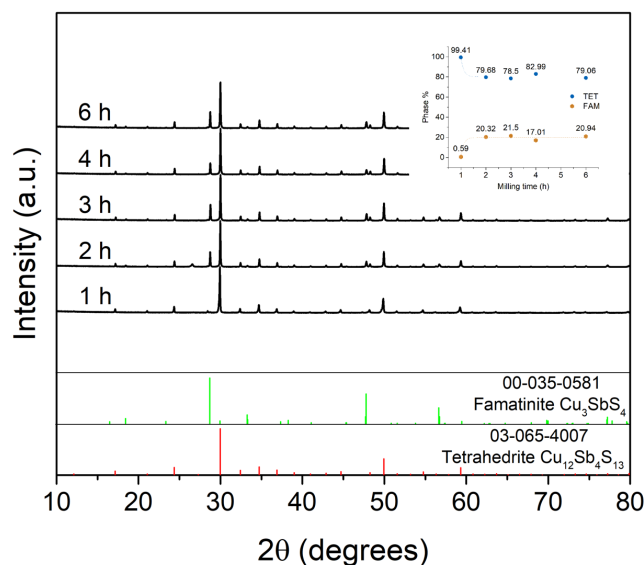


Figure 1. XRD patterns of sintered samples versus milling time. Inset: relative ratio of tetrahedrite (●) to famatinite (●) determined from Rietveld refinement.

3.2. Conversion degree of mechanochemical synthesis

The amount of non-reacted elemental sulphur has been determined by the Soxhlet method in order to evaluate the extent of mechanochemical synthesis. The data for conversion degree α calculated according to equation (1) are given in supplementary information (**Table S2**). Definitely, the total conversion to binary and ternary sulphides is very fast, as the only small amounts of non-reacted sulphur were detected. Consequently, the conversion degree calculated for the milling interval 1-6 h is very high and approaches 98-99 %.

3.3. XPS analysis

XPS analyses were carried out to determine the composition of the surface species in mechanochemically synthesized sulphides. The XPS patterns were investigated in detail and are displayed in **Figure 2** for M1 and M1S samples, and **Figure S3** for M3 and M3S samples. The spectra for Cu $2p$, Sb $3d$, and S $2p$ were recorded in a high-resolution core level mode. Based on the binding energy values, a peak splitting (PS) was also calculated. The values of PS play a decisive role in the determination of the oxidation states of the elements on the surfaces. XPS can especially offer resolved spectra for Cu^+ and Cu^{2+} species, respectively [72].

Bearing in mind the distribution of species in the compounds (see **Figs. 1 and S2** and **Table 2**), the following oxidation states can be expected : Cu^{1+} for famatinite [73], covellite [73] and tetrahedrite [4, 73], Cu^{2+} for tetrahedrite [4, 73], Sb^{5+} for famatinite [74], Sb^{3+} for tetrahedrite and skinnerite [7-8, 74] and S^{2-} for all sulphidic species [7-8, 73, 74].

Four samples have been selected for XPS analysis, *i.e.* M1, M3, M1S and M3S, where M denotes a milled sample and MS is the same sample subsequently sintered by SPS. The milling time for samples M1 and M1S was 1 hour, for samples M3 and M3S was 3 hours.

For copper atoms, the values of binding energies of 952.83 eV, 933.08 eV for M1 and of 953.10 eV, 933.09 eV for M3 were calculated by peak fitting (see **Fig. 2a** and **Fig. S3a**). Comparably, PS values of 19.8 eV and 20.0 eV for both samples confirm the presence of Cu^{+1} state. Accordingly, the values of 953.17 eV, 933.22 eV for M1S and of 953.23 eV, 933.37 eV for M3S correspond with the values of PS 20.0 eV and 19.9 eV. The values of binding energies for both sintered samples are in good agreement with the values for Cu^{1+} given in [4, 72-76]. In agreement with the corresponding XRD patterns in **Fig. 1 and S2**, and the phases reported in **Table 2**, the presence of Cu^{1+} can be connected with covellite, skinnerite, famatinite and tetrahedrite. The SPS treatment has not a detrimental effect on the presence of Cu^{1+} . However, the satellites with binding energies 942.91 eV, 943.69 eV and 942.78 eV can be traced in the samples M1S, M3 and M3S (**Fig. 2d, S3a and S3d**). Because Cu^{2+} is present only in tetrahedrite

[4, 73], this satellite peak can be associated with this phase. The absence of Cu^{2+} in sample M1 can be associated with the lowest content of tetrahedrite in comparison with samples M1S, M3 and M3S.

XPS spectra for Sb $3d$ are depicted in **Fig. 2b** and **Fig. S3b** for milled samples (M) and in **Fig. 2e** and **Fig. S3e** for the sintered samples by SPS (MS). In all the figures, two intensive peaks corresponding to $3d_{5/2}$ and $3d_{3/2}$ states of antimony are present. Their Eb values are in the regions (539.43-540.57) eV for $3d_{5/2}$ state and (530.64-531.43) eV for $3d_{3/2}$ state. The peak separation ($3d_{5/2}$ and $3d_{3/2}$) originates from spin-orbit coupling. Peaks can be connected with Sb^{3+} state [77] corresponding to tetrahedrite and skinnerite. However, we hypothesize that Sb^{5+} can be also present as a consequence of famatinite [74].

XPS spectra for S $2p$ are depicted in **Figs. 2c** and **S3c** for milled samples and in **Fig. 2f** and **Fig. S3f** for the sintered samples by SPS (MS). The values of binding energies in the region (162.46-163.95) eV belong to the states $\text{S}2p_{3/2}$ and $\text{S}2p_{1/2}$ and correspond very well with the expected values for S^{2-} oxidation state [73, 78]. However, also small hallos can be traced for the milled samples M1 and M3 (**Figs. 2c** and **S3c**) with maximum at binding energy of ~ 169 eV, which is characteristic value of S^{6+} oxidation state [79]. After SPS treatment, in samples M1S and M3S (**Figs. 2f** and **S3f**), these hallos are missing. This illustrates the positive influence of the SPS treatment on the purification and surface stability of the samples in this study.

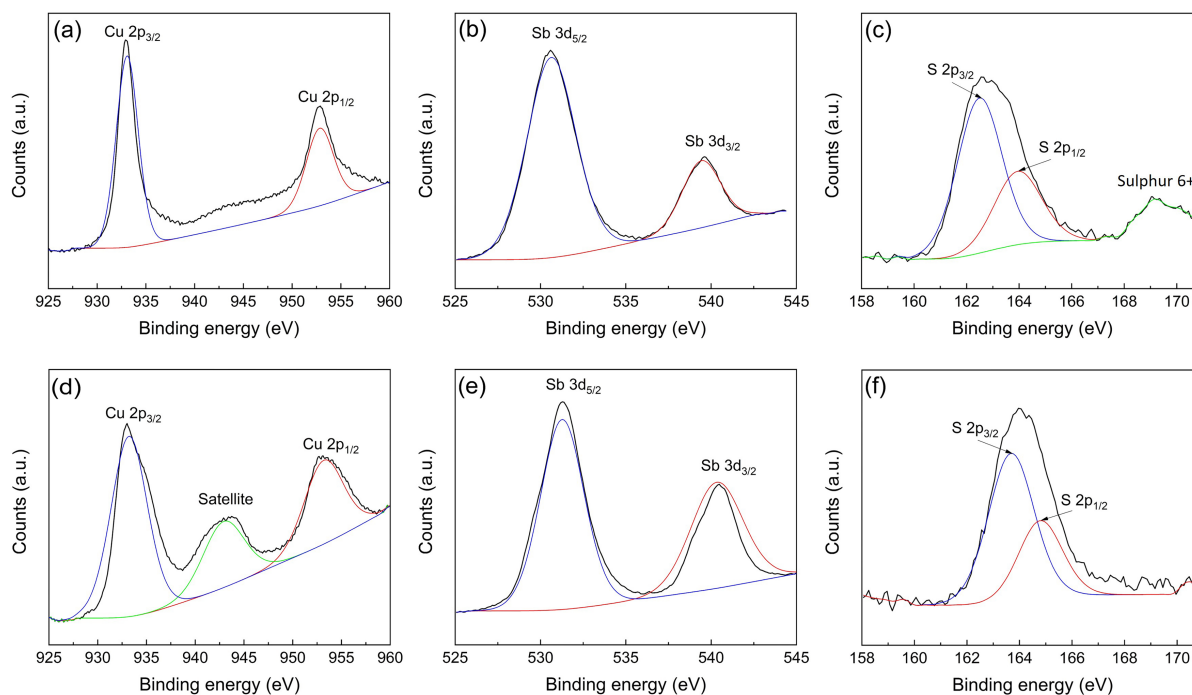


Figure 2. High-resolution spectra of M1 (a,b,c) and M1S (d,e,f) samples: (a,d) Cu $2p$, (b,e) Sb $3d$, (c,f) S $2p$. Milling time of 1h.

3.4. SEM and TEM analysis

SEM images of mechanochemically synthesized powders are given in **Fig. S4**. Polydisperse distribution of grains can be observed with the tendency to form aggregated particles. The same observation was reported in [55] where the obtained tetrahedrite particles decreased significantly to several micrometers in comparison with the size of tenths micrometers of the reaction precursors. By synthesis from salts in an autoclave, particles of $\text{Cu}_{12}\text{Sb}_4\text{S}_{13}$ with an average diameter of 50-70 nm were obtained [77]. However, nanoparticles can also be detected in our case in the form of aggregated grains, with particle sizes of several hundreds of nanometers. No significant difference is observed between the two powders.

SPS treated powders after milling for 1h and 3h were further analysed by SEM to reveal the microstructural characteristics (**Figure 3**). The M1S sample contains only tetrahedrite, while

the M3S sample is a mixture of two phases, tetrahedrite and famatinite, as already determined by XRD (see diffraction pattern in **Fig. 1**).

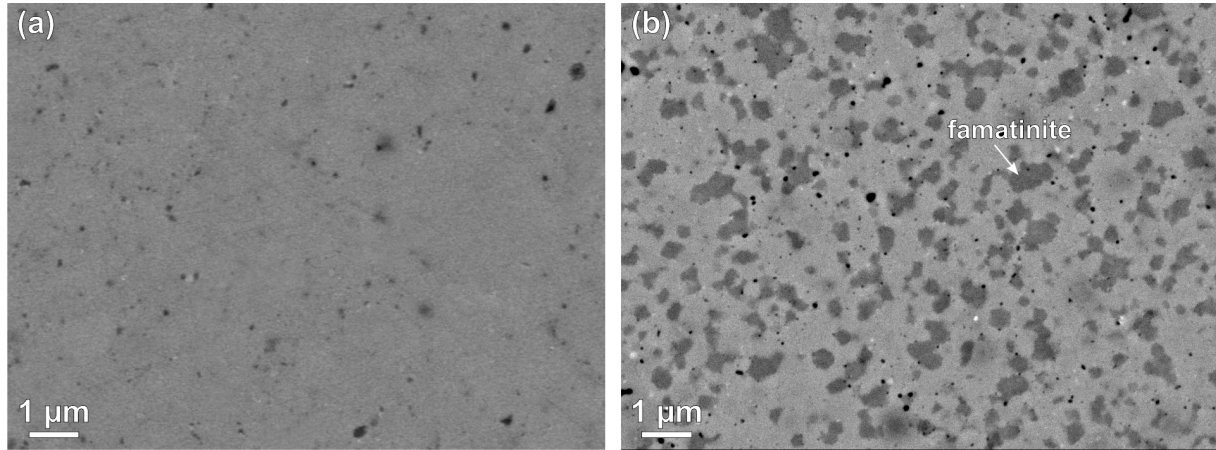


Figure 3. SEM images of sintered samples from a) 1h ball-milling (M1S) and b) 3h ball-milled (M3S) powder.

Both samples are fully densified and contain only a few closed pores with diameter well below micron. SEM/EDS analysis of the M1S sample shows that the sample has a homogenous chemical composition with Cu:Sb:S atomic ratio close to the theoretically expected ratio for tetrahedrite ($\text{Cu} : \text{Sb} : \text{S} = 39.0 \pm 0.2 : 14.4 \pm 0.1 : 46.6 \pm 0.1$). The sample contains also nanosized WC particles (bright contrast in backscattered SEM figures) inside the tetrahedrite matrix. The presence of these particles is a consequence of wear from milling balls composed of tungsten carbide WC. In contrast to the M1S sample, the M3S sample clearly contains tetrahedrite and famatinite, showing brighter and darker contrast in backscattered SEM images, respectively. EDS analysis of the darker areas has shown a relatively higher amount of sulphur and lower amounts of Cu and Sb compared to the areas with brighter contrast as expected for famatinite. The ratio between the brighter and darker areas in the sample, *i.e.* the tetrahedrite to famatinite ratio determined from SEM images is approximately 77:23, which is in good agreement with the results of XRD analyses. Famatinite is homogeneously distributed among

tetrahedrite and the transversal and longitudinal cross-sections of the sintered compact have shown identical microstructures indicating that the sample is not textured.

The M3S sample was additionally investigated by TEM. **Fig. 4a** is a typical low-magnification bright-field (BF) image showing tightly compacted tetrahedrite grains with nearly isometric morphology and fairly uniform grain size with a diameter between 200 and 500 nm. TEM images also reveal the presence of nanosized pores trapped at the grain boundaries (**Figs. 4a** and **4b**). Magnified detail across the contact of four tetrahedrite grains reveals direct contacts between the grains without any amorphous layer at the contact. The chemical composition of grains and grain boundaries was inspected by TEM/EDS, however, due to an additional signal of Cu from the brass supporting ring, only relative comparison between EDS spectra taken a few nanometers apart at the same acquisition conditions was possible. The analyses have shown that there is no significant difference in the chemical composition of grain boundaries in comparison to the neighboring tetrahedrite grains, only the slightly increased amount of Sb at some grain boundaries was detected.

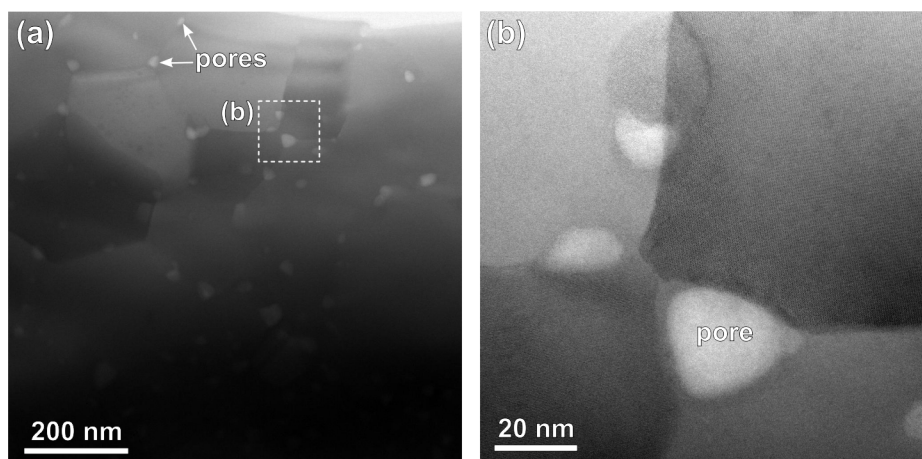


Figure 4. (a) Low-magnification BF-STEM image of M3S sample showing tetrahedrite grains with nanosized pores at grain boundaries. (b) Contact of four tetrahedrite grains with pores trapped at the contacts; BF-STEM image.

The presence of the famatinite phase in the M3S sample was also investigated in more detail by TEM. **Fig. 5a** shows a typical famatinite grain embedded in the matrix of tetrahedrite grains. The size of the famatinite grains is comparable to the tetrahedrite grains. The grain shown in Figure 8b is oriented along the $[-221]$ zone axis as determined from the fast Fourier transform (FFT) of the high-resolution DF and BF STEM images shown in **Fig. 5b**.

The presence of nanosized pores along with copper and carbon enrichment at grain boundaries together with famatinite inclusions can be directly correlated with thermoelectric properties of the samples. Generally, this nanostructuring effect and locally inhomogeneous local structure is a predisposition for lowering thermal conductivity as described earlier [40-45].

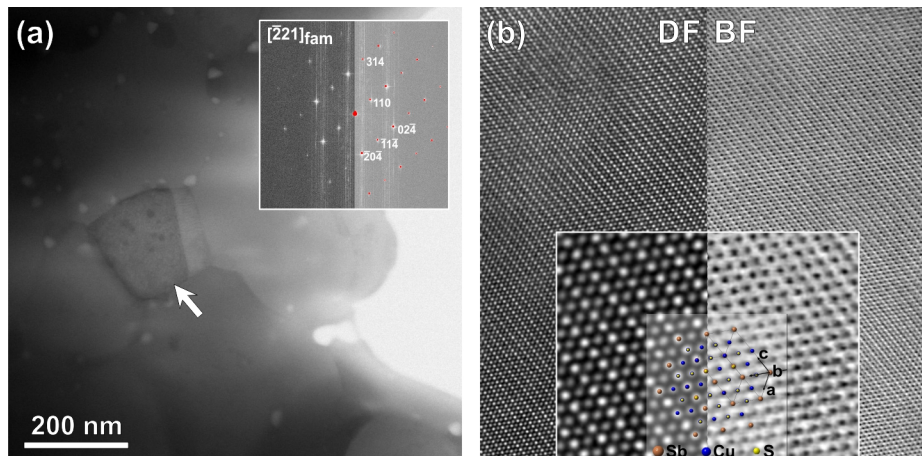


Figure 5. (a) Famatinite grain (arrow) in the matrix of tetrahedrite grains. FFT pattern in the inset (upper right) calculated from the high-resolution images shown in (b) for determination of the crystal orientation. (b) A pair of dark-field (DF) and bright-field (BF) atomic resolution STEM images with enlarged detail in the bottom part of the figure and superimposed crystal structure model of famatinite along $[-221]$ zone axis.

3.5. Thermoelectric properties

The temperature dependences of electrical conductivity (σ), Seebeck coefficient (S), power factor (PF), total thermal conductivity (κ) and figure-of-merit (zT) were collected on sintered

samples over the temperature range 300-700 K. In **Fig. 6a**, the electrical conductivity of all the samples exhibits a semiconducting behaviour with a clear transition to a metal-like behaviour at 550 K. This behaviour was already reported in several other studies on pristine tetrahedrites [24,27]. A marked difference can be observed between M1S sample and the four other samples. M1S sample exhibit a lower electrical conductivity as compared to the four other samples, in agreement with the presence of famatinite in a large content in M2S, M3S, M4S, and M6S samples. Although the famatinite phase is known as a semiconductor characterized by a low electrical conductivity [69, 70], the larger electrical conductivity in samples containing famatinite phase is likely explained by stoichiometry deviations in the tetrahedrite phase. Indeed, variations of the composition of the crystal structure induce a change in the carrier concentration, which is supported by the marginally lower Seebeck coefficient in M2S-M6S samples on the full temperature range (**Fig. 6b**). In addition, the magnitude of the Seebeck coefficient at RT for the five samples remains close to the ones reported for pristine tetrahedrite [24, 27, 35].

The changes in electrical conductivity and Seebeck coefficient are in overall counterbalanced, leading to similar power factor values on the overall temperature for the five samples. The highest value of around $1.05 \text{ mW m}^{-1} \text{ K}^{-2}$ at 700 K is achieved for M1S and M2S samples. Comparison with other works shows that values obtained in this work are in good agreement with the pristine tetrahedrites prepared by mechanochemical and high-temperature synthesis [24, 56, 80-81].

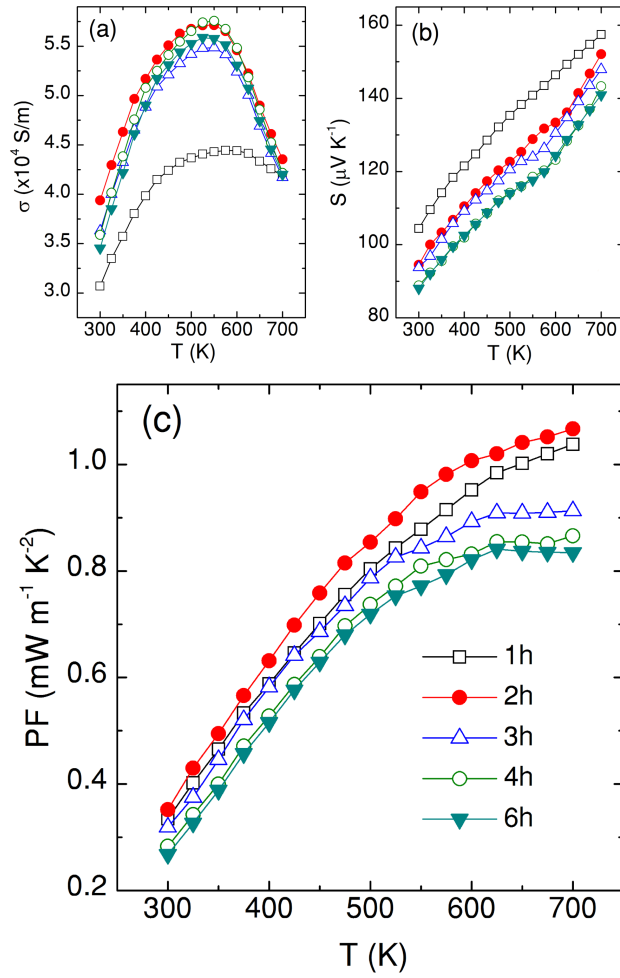


Figure 6. Temperature dependence of (a) electrical conductivity σ , (b) Seebeck coefficient S , and (c) power factor PF , of sintered samples for different milling times.

The temperature dependences of the thermal conductivity are displayed in **Fig. 7a**. For M1S sample, the thermal conductivity increases with temperature in agreement with previous reports on pristine tetrahedrite [24, 27, 35]. The magnitude is comparable to the ones observed in other pristine tetrahedrites prepared by mechanical-alloying or by high-temperature synthesis [24, 27, 28, 35, 82, 83]. For the other four samples (M2S-M6S), the thermal conductivity decreases with the increasing temperature with an abrupt deflection at 375 K. The jump observed in the temperature dependence of the thermal conductivity around 375 K is not yet understood but

may be caused by an exsolution process or reactivity between famatinite and tetrahedrite. The larger values observed in famatinite rich samples is explained by the increased electronic contribution in those samples (increased electrical conductivity) and by the enhanced lattice thermal conductivity (inset of **Fig. 7a**) due to the larger lattice thermal conductivity of famatinite [69-70] as compared to tetrahedrite.

For the sample milled for 1 h (M1S), the combination of relatively high PF ($1.07 \text{ mW m}^{-1} \text{ K}^{-2}$ at 700 K) and low thermal conductivity ($1.12 \text{ W m}^{-1} \text{ K}^{-1}$ at 700 K) leads to the highest figure-of-merit ZT (0.67 at 700 K) among the investigated samples, which is comparable with values reported for undoped tetrahedrites synthesized using laboratory mechanochemical [56, 80] and high-temperature synthesis [23, 35, 81, 82].

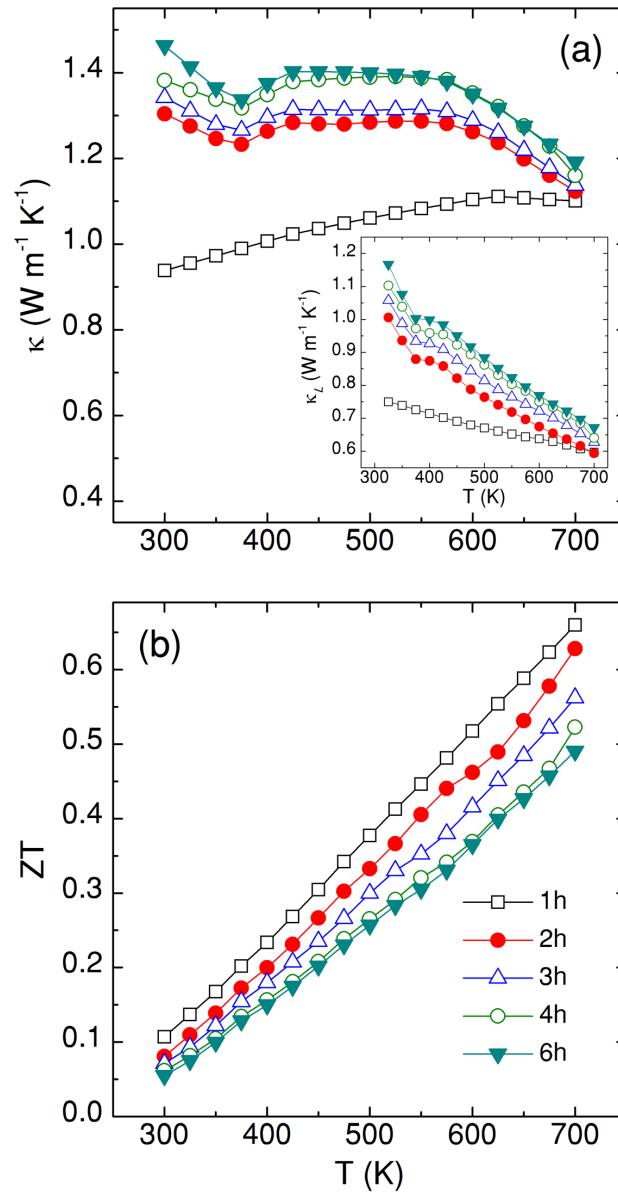


Figure 7. Temperature dependence of (a) thermal conductivity κ and (b) figure-of-merit ZT of sintered samples for different milling times. Inset in (a) displays the temperature dependence of the lattice thermal conductivity.

4. CONCLUSIONS

In this work, tetrahedrite $\text{Cu}_{12}\text{Sb}_4\text{S}_{13}$ was synthesized in an industrial vibratory mill. The milling was performed up to 6h in an argon atmosphere using Cu, Sb, and S as elemental precursors. After milling the samples were treated by spark plasma sintering (SPS). Methods of XRD,

Soxhlet analysis, XPS, SEM, EDS, TEM and thermoelectric analysis were applied to characterize properties of the synthesized products. Mechanochemical synthesis in industrial mill proceeds via several intermediate phases where skinnerite (Cu_3SbS_3) together with famatinite (Cu_4SbS_4) and tetrahedrite ($\text{Cu}_{12}\text{Sb}_4\text{S}_{13}$) are prevailing. However, the product is chemically more uniform after SPS treatment. For example, the sample milled for 1 h and subsequently SPS treated is almost exclusively tetrahedrite. Soxhlet analysis showed the total conversion of the applied mechanochemical reaction. XPS analysis allowed us to discriminate between Cu^{1+} , Cu^{2+} , Sb^{3+} and Sb^{5+} species in tetrahedrite and famatinite. Nanosize particles were identified by SEM and HRTEM methods. In the latter case, dimensions around 250 nm for tetrahedrite were determined. The thermoelectric measurements performed for optimal sample (milling time 60 min) revealed a figure-of-merit value ZT of $0.67@700\text{K}$ as a consequence of relatively high power factor ($1.07 \text{ mW m}^{-1} \text{ K}^{-2}$) and low thermal conductivity ($1.12 \text{ W m}^{-1} \text{ K}^{-1}$). The obtained ZT value for tetrahedrite powders synthesized in an industrial mill is comparable to the values obtained in laboratory mills. The synthesized ternary sulphide represents a prospective material for future applications. The applied approach can serve as a scalable route for the preparation of ternary and quaternary sulphides for a wide range of applications.

ACKNOWLEDGEMENT

This work was supported by the Slovak Research and Development Agency (project APVV-18-0357) and the Slovak Grant Agency (projects VEGA 2/0044/18, 2/0065/18). The support of the European research project COST (OC-2015-1-19345) is also acknowledged. O.D. thanks to the National Scholarship Programme of the Slovak Republic (SAIA) for his research grant performed at the Institute of Geotechnics of Slovak Academy of Sciences. The technical support

for XRF and surface analyses performed by Dr. Šestinová and Dr. Lukáčová Bujňáková is also acknowledged.

SUPPORTING INFORMATION

Figure S1. a) industrial mill with the attached closed satellite chamber, b) open satellite chamber without milling balls and c) milling balls.

Figure S2. XRD patterns of mechanochemically synthesized powders versus milling time (h).

Figure S3. High-resolution spectra of M3 (a,b,c) and M3S (d,e,f) samples: (a,d) Cu 2*p*, (b,e) Sb 3*d*, (c,f) S 2*p*. Milling time of 3h.

Figure S4. SEM images of powders ball-milled for 1h (a,b) and 3h (c,d).

Table S1. Thermoelectric properties of Cu₁₂Sb₄S₁₃ tetrahedrite material obtained by the different synthetic and consolidation methods.

Table S2. Soxhlet analysis of samples after milling.

5. REFERENCES

- [1] P. Baláž, *Extractive Metallurgy of Activated Minerals*, Elsevier, Amsterdam, 2000.
- [2] P. Baláž, *Mechanochemistry in Nanoscience and Minerals Engineering*, Springer, Berlin, 2008.
- [3] K. Suekuni, K. Tsuruta, T. Ariga, M. Koyano, Thermoelectric properties of mineral tetrahedrites $\text{Cu}_{10}\text{Tr}_2\text{Sb}_4\text{S}_{13}$ with low thermal conductivity. *Appl. Phys. Express.* 5 (2012) 051201.
- [4] R.A.D. Patrick, A.J. Hall, Silver substitution into synthetic zinc, cadmium, and iron tetrahedrites, *Mineral. Mag.* 47 (1983) 441-451.
- [5] N.E. Johnson, J.R. Craig, J. Donald Rimstidt, Crystal chemistry of tetrahedrite, *Am. Mineral.* 73 (1988) 389-397.
- [6] E. Makovicky, K. Moller, Exploratory studies on substitution of minor elements in synthetic tetrahedrite, *Neu. Jb. Mineral. - Abh.* 167 (1994) 89-123.
- [7] R. Chetty, A. Bali, R.C. Mallik, Tetrahedrites as thermoelectric materials: an overview, *J. Mater. Chem.* 3 (2015) 12364-12378.
- [8] R. Chetty, D.S. Prem Kumar, G. Rogl, P. Rogl, E. Bauer, H. Michor, S. Suwas, S. Puchegger, G. Giester, R.C. Mallik, Thermoelectric properties of a Mn substituted synthetic tetrahedrite, *Phys. Chem. Chem. Phys.* 17 (2015) 1716-1727.
- [9] B.J. Wuensch, Confirmation of the crystal structure of tetrahedrite $\text{Cu}_{12}\text{Sb}_4\text{S}_{13}$, *Science* 14 (1963) 804-805.
- [10] B.J. Wuensch, The crystal structure of tetrahedrite $\text{Cu}_{12}\text{Sb}_4\text{S}_{13}$, *Z. Krist.-Cryst. Mater.* 119 (1964) 437-453.
- [11] M. Telkes, Thermoelectric power and electrical resistivity of minerals, *Am. Mineral.* 35 (1950) 536-555.

- [12] X. Lu, Thermoelectric Properties of Natural Mineral Based Tetrahedrite Compounds, PhD thesis, Michigan State University, 2014.
- [13] Y. Bouyrie, Identification, Synthèse et Caractérisation de Phases Tetraédrites pour la Conversion d'énergie par effets thermoélectriques, PhD thesis, Université de Lorraine, 2015.
- [14] K. Chen, Synthesis and Thermoelectric Properties of Cu-Sb-S Compounds, PhD thesis, Queen University of London, 2016.
- [15] G.P.L. Guélou, On the Structural and Physical Properties of Earth-Abundant Sulphides for Thermoelectric Applications, PhD thesis, University of Reading, 2016.
- [16] P. Levinský, Synthesis, Characterization and Optimization of New Thermoelectric Materials, PhD thesis, Czech Technical University Prague and Université de Lorraine, 2018.
- [17] C. Candolfi, Y. Bouyrie, S. Sassi, A. Dauscher, B. Lenoir, Prospective novel thermoelectric materials, in: S. Skipidarov, M. Nikitin (Eds.), Thermoelectrics for Power Generation - A Look at Trends in the Technology, InTechOpen, 2016, pp. 71-89.
- [4] G.R. Mettam, L.B. Adams, How to prepare an electronic version of your article, in: B.S. Jones, R.Z. Smith (Eds.), Introduction to the Electronic Age, E-Publishing Inc., New York, 2009, pp. 281–304.
- [18] S. Hébert, D. Berthebaud, R. Daou, Y. Bréard, D. Pelloquin, E. Guilmeau, F. Gascoin, O. Lebedev, A. Maignan. Searching for new thermoelectric materials: some examples among oxides, sulfides and selenides. *J. Phys. Condens. Matter.* 28 (2016) 013001.
- [19] K. Suekuni, T. Takabatake. Research update: Cu-S based synthetic minerals as efficient thermoelectric materials at medium temperatures. *APL Mater.* 4 (2016) 104503.
- [20] W. Lai, Y. Wang, D.T. Morelli, X. Lu, From bonding asymmetry to anharmonic rattling in $\text{Cu}_{12}\text{Sb}_4\text{S}_{13}$ tetrahedrites: when lone-pair electrons are not so lonely, *Adv. Funct. Mater.* 25 (2015) 3648-3657.

- [21] Y. Bouyrie, C. Candolfi, S. Pailhès, M.M. Koza, B. Malaman, A. Dauscher, J. Tobola, O. Boisron, L. Saviot, B. Lenoir, From crystal to glass-like thermal conductivity in crystalline minerals, *Phys. Chem. Chem. Phys.* 17 (2015) 19751-19758.
- [22] K. Suekuni, C. Ho Lee, H.I. Tanaka, E. Nishibori, A. Nakamura, H. Kasai, H. Mori, H. Usui, M. Ochi, T. Hasegawa, M. Nakamura, S. Ohira-Kawamura, T. Kikuchi, K. Kaneko, H. Nishiate, K. Hashikuni, Y. Kosaka, K. Kuroki, T. Takabatake. Retreat from stress: rattling in planar coordination. *Adv. Mater.* 30 (2018) 1706230.
- [23] D.S. Prem Kumar, R. Chetty, O.E. Femi, K. Chattopadhyay, P. Malar, R.C. Mallik, Thermoelectric properties of Bi doped tetrahedrite, *J. Electron. Mater.* 46 (2017) 2616-2622.
- [24] T. Barbier, P. Lemoine, S. Gascoin, O.I. Lebedev, A. Kaltzoglou, P. Vaqueiro, A.V. Powell, R.I. Smith, E. Guilmeau, Structural stability of the synthetic thermoelectric ternary and nickel-substituted tetrahedrite phases, *J. Alloys Compd.* 634 (2015) 253-262.
- [25] T. Barbier, S. Rolli-Martinet, P. Lemoine, F. Gascoin, A. Kaltzoglou, P. Vaqueiro, A.V. Powell, E. Guilmeau, Thermoelectric materials: a new rapid synthesis process for nontoxic and high-performance tetrahedrite compounds, *J. Am. Ceram. Soc.* 99 (2016) 51-56.
- [26] X. Lu, D.T. Morelli, Rapid synthesis of high-performance thermoelectric materials directly from natural mineral tetrahedrite, *MRS Commun.* 3 (2013) 129-133.
- [27] X. Lu, D.T. Morelli, Y. Xia, F. Zhou, V. Ozolins, H. Chi, X. Zhou, C. Uher, High performance thermoelectricity in earth-abundant compounds based on natural mineral tetrahedrites, *Adv. Energy Mater.* 3 (2013) 342-348.
- [28] X. Lu, D. Morelli, The effect of Te substitution for Sb on thermoelectric properties of tetrahedrite, *J. Electron. Mater.* 43 (2013) 1983-1987.
- [29] X. Lu, D.T. Morelli, Natural mineral tetrahedrite as a direct source of thermoelectric materials, *Phys. Chem. Chem. Phys.* 15 (2013) 5762-5766.

- [30] D.P. Weller, D.T. Morelli, Rapid synthesis of zinc and nickel co-doped tetrahedrite thermoelectrics by reactive spark plasma sintering and mechanical alloying, *J. Alloys Compd.* 710 (2017) 794-799.
- [31] A.P. Gonçalves, E.B. Lopes, B. Villeroy, J. Monnier, C. Godart, B. Lenoir, Effect of Ni, Bi and Se on the tetrahedrite formation, *RSC Adv.* 6 (2016) 102359-102367.
- [32] A.P. Gonçalves, E.B. Lopes, J. Monnier, E. Alleno, C. Godart, M.F. Montemor, J.B.S. Vaney, B. Lenoir, Tetrahedrites for low cost and sustainable thermoelectrics, *Solid State Phenom.* 275 (2017) 135-138.
- [33] K. Chen, B. Du, N. Bonini, C. Weber, H. Yan, M.J. Reece, Theory-guided synthesis of an eco-friendly and low-cost copper based sulfide thermoelectric material, *J. Phys. Chem. C* 120 (2016) 27135-27140.
- [34] J. Heo, G. Laurita, S. Muir, M.A. Subramanian, D.A. Keszler, Enhanced thermoelectric performance of synthetic tetrahedrite, *Chem. Mater.* 26 (2014) 2047-2051.
- [35] K. Suekuni, K. Tsuruta, M. Kunii, H. Nishiate, E. Nishibori, S. Maki, M. Ohta, A. Yamamoto, M. Koyano. High-performance thermoelectric mineral $\text{Cu}_{12-x}\text{Ni}_x\text{Sb}_4\text{S}_{13}$ tetrahedrite. *J. Appl. Phys.* 4 (2013) 043712.
- [36] K. Suekuni, Y. Tomizawa, T. Ozaki, M. Koyano. Systematic study of electronic and magnetic properties for $\text{Cu}_{12-x}\text{TM}_x\text{Sb}_4\text{S}_{13}$ (TM = Mn, Fe, Co, Ni and Zn). *J. Appl. Phys.* 115 (2014) 143702.
- [37] S. Fasolin, S. Fiameni, C. Fanciulli, S. Battiston, A. Famengo, M. Fabrizio, Nanostructured tetrahedrite synthesis for thermoelectric applications, *J. Nanosci. Nanotechnol.* 17 (2017) 1645-1648.
- [38] X. Lu, D.T. Morelli, Y. Xia, V. Ozolins, Increasing the thermoelectric figure of merit of tetrahedrites by co-doping with nickel and zinc, *Chem. Mater.* 27 (2015) 408-413.

- [39] T. Barbier, P. Lemoine, S. Martinet, M. Eriksson, M. Gilmas, E. Hug, G. Guélou, P. Vaqueiro, A.V. Powell, E. Guilmeau. Up-scaled synthesis process of sulphur-based thermoelectric materials. *RSC Adv.* 6 (2016) 10044.
- [40] M.S. Dresselhaus, G. Chen, M.Y. Tang, R.G. Yang, H. Lee, D.Z. Wang, Z.F. Ren, J.P. Fleurial, P. Gogna, New directions for low-dimensional thermoelectric materials. *Adv. Mater.* 19 (2007) 1043-1053.
- [41] G.J. Snyder, E.S. Toberer, Complex thermoelectric materials, *Nat. Mater.* 7 (2008) 105-144.
- [42] P. Vaqueiro, A.V. Powell, Recent developments in nanostructured materials for high-performance thermoelectrics, *J. Mater. Chem.* 20 (2010) 9577-9584.
- [43] M.G. Kanatzidis, Nanostructured thermoelectrics: the new paradigm? *Chem. Mater.* 22 (2010) 648-659.
- [44] Y. Lan, A.J. Minnich, G. Chen, Z. Ren, Enhancement of thermoelectric figure-of-merit by a bulk nanostructuring approach, *Adv. Funct. Mater.* 20 (2010) 357-376.
- [45] J.P. Heremans, M.D. Dresselhaus, L.E. Bell, D.T. Morelli, When thermoelectrics reached the nanoscale, *Nat. Nanotechnol.* 8 (2013) 471-473.
- [46] P. Baláž, M. Baláž, M. Achimovičová, Z. Bujňáková, E. Dutková, Chalcogenide mechanochemistry in materials science: insight into synthesis and applications (a review), *J. Mater. Sci.* 52 (2017) 11851-11890.
- [47] P. Baláž, M. Baláž, M.J. Sayagués, A. Eliyas, N.G. Kostova, M. Kaňuchová, E. Dutková, A. Zorkovská, 2017. Chalcogenide quaternary nanocrystals for solar cells: explosive character of mechanochemical synthesis and environmental challenge. *Crystals* 7 (2017) 367.
- [48] M. Baláž, A. Zorkovská, J.S. Blazquez, N. Daneu, P. Baláž, Mechanochemistry of copper sulphides: phase interchanges during milling, *J. Mater. Sci.* 52 (2017) 11947-11961.

- [49] T. Frišćić, New opportunities for materials synthesis using mechanochemistry, *J. Mater. Chem.* 20 (2010) 7599-7603.
- [50] V. Šepelák, K.D. Becker, Mechanochemistry: from mechanical degradation to novel materials properties, *J. Korean Ceram. Soc.* 49 (2012) 19-28.
- [51] S.L. James, C.J. Adams, C. Bolm, D. Braga, P. Collier, T. Frišćić, F. Grepioni, K.D.M. Harris, G. Hyett, W. Jones, A. Krebs, J. Mack, L. Maini, A.G. Orpen, I.P. Parkin, W.C. Shearouse, J.W. Steed, D.C. Waddell, Mechanochemistry: opportunities for new and cleaner synthesis, *Chem. Soc. Rev.* 41 (2012) 413-447.
- [52] E. Boldyreva, Mechanochemistry of inorganic and organic systems: what is similar, what is different?, *Chem. Soc. Rev.* 42 (2013) 7719-7738.
- [53] W. Jones, M.D. Eddleston, Introductory lecture: mechanochemistry, a versatile synthesis strategy for new materials, *Faraday Discuss.* 170 (2014) 9-34.
- [54] J.L. Do, T. Frišćić, Mechanochemistry: a force of synthesis, *ACS Cent. Sci.* 3 (2017) 13-19.
- [55] P. Baláž, M. Achimovičová, M. Baláž, P. Billik, Z. Cherkezova-Zheleva, J.M. Criado, F. Delogu, E. Dutková, E. Gaffet, F.J. Gotor, R. Kumar, I. Mitov, T. Rojac, M. Senna, A. Streletskii, K. Wiczorek-Ciurawa, Hallmarks of mechanochemistry: from nanoparticles to technology, *Chem. Soc. Rev.* 42 (2013) 7571-7637.
- [56] S.-Y. Kim, S.-G. Kwak, J.-H. Pi, G.-E. Lee, I.-H. Kim, Preparation of tetrahedrite $\text{Cu}_{12}\text{Sb}_4\text{S}_{13}$ by mechanical alloying and hot pressing, *J. Electron. Mater.* 48 (2019) 1857-1863.
- [57] J.-H. Pi, G.-E. Lee, I.-H. Kim, Effect of aging on thermoelectric properties of tetrahedrite $\text{Cu}_{12}\text{Sb}_4\text{S}_{13}$, *J. Korean Phys. Soc.* 74 (2019) 865-870.
- [58] J. Rodriguez-Carvajal, Fullprof program, version 2.4.2, Grenoble, France, 1993.
- [59] Joint Committee on Powder Diffraction Standards (JCPDS), Powder diffraction file (PDF), International Centre for Diffraction Data, Newtown Square, 2004.

- [60] H.-S. Kim, Z.M. Gibbs, Y. Tang, H. Wang, G. J. Snyder. Characterization of Lorenz number with Seebeck coefficient measurement. *APL Mater.* 3 (2015) 041506.
- [61] E. Alleno, D. Bérardan, C. Byl, C. Candolfi, R. Daou, R. Decourt, E. Guilmeau, S. Hébert, J. Hejtmanek, B. Lenoir, P. Masschelein, V. Ohorodnichuk, M. Pollet, S. Populoh, D. Ravot, O. Rouleau, M. Soulier. A round Robin test of the uncertainty on the measurements of the thermoelectric dimensionless figure of merite of $\text{Co}_{0.97}\text{Ni}_{0.03}\text{Sb}_3$. *Rev. Sci. Instrum.* 86 (2015) 011301.
- [62] M. Baláž, N. Daneu, M. Rajňák, J. Kurimský, M. Hegedüs, E. Dutková, M. Fabian, M. Kaňuchová, P. Baláž, Rapid mechanochemical synthesis of nanostructured mohite Cu_2SnS_3 (CTS), *J. Mater. Sci.* 53 (2018) 13631-13642.
- [63] E. Dutková, Z. Bujňáková, J. Kováč, I. Škorvánek, M.J. Sayagués, A. Zorkovská, J. Kováč Jr., P. Baláž, Mechanochemical synthesis, structural, magnetic and electrooptical properties of CuFeS_2 nanoparticles, *Adv. Powder Technol.* 29 (2018) 1820-1826.
- [64] M. Hegedüs, P. Baláž, M. Baláž, P. Siffalovic, N. Daneu, M. Kaňuchová, J. Briančin, M. Fabián, Mechanochemical approach to a $\text{Cu}_2\text{ZnSnS}_4$ solar cell absorber via a “micro-nano” route, *J. Mater. Sci.* 53 (2018) 13617-13630.
- [65] P. Baláž, M. Hegedüs, M. Achimovičová, M. Baláž, M. Tešínský, E. Dutková, M. Kaňuchová, J. Briančin, Semi-industrial green mechanochemical syntheses of solar cell absorbers based on quaternary sulfides, *ACS Sustainable Chem. Eng.* 6 (2018) 2132-2141.
- [66] M. Baláž, A. Zorkovská, F. Urakaev, P. Baláž, J. Briančin, Z. Bujňáková, M. Achimovičová, E. Gock, Ultrafast mechanochemical synthesis of copper sulfides, *RSC Adv.* 6 (2016) 87836-87842.
- [67] J.R. Craig, P.B. Barton, Thermochemical approximations for sulfosalts, *Econ Geol.* 68 (1973) 493-506.

- [68] K. Tatsuka, N. Morimoto, Tetrahedrite stability relations in the Cu-Sb-S system, *Econ. Geol.* 72 (1977) 258-270.
- [69] K. Chen, C. Di Paola, B. Du, R. Zhang, S. Laricchia, N. Bonini, C. Weber, I. Abrahams, H. Yan, M. Reece, Enhanced thermoelectric performance of Sn-doped Cu_3SbS_4 , *J. Mater. Chem. C*, 6 (2018) 8546-8552.
- [70] A. Suzumura, M. Watanabe, N. Nagasako, R. Asahi, Improvement in thermoelectric properties of Se-free Cu_3SbS_4 compound, *J. Electron. Mater.* 43 (2014) 2356-2361.
- [71] B. Du, K. Chen, H. Yan, M.J. Reece, Efficacy of lone-pair electrons to engender ultralow thermal conductivity, *Scr. Mater.* 111 (2016) 49-53.
- [72] T.K. Le, D. Flahaut, H. Martinez, N. Andreu, D. Gonbeau, E. Pachoud, D. Pelloquin, A. Maignan, The electronic structure of the $\text{CuRh}_{1-x}\text{Mg}_x\text{O}_2$ thermoelectric materials: An X-ray photoelectron spectroscopy study, *J. Solid State Chem.* 184 (2011) 2387
- [73] J. van Embden, K. Latham, N.W. Duffy, Y. Tachibana, Near-infrared absorbing $\text{Cu}_{12}\text{Sb}_4\text{S}_{13}$ and Cu_3SbS_4 nanocrystals: synthesis, characterization, and photoelectrochemistry, *J. Amer. Chem. Soc.* 135 (2013) 11564-11571.
- [74] L. Wang, B. Yang, Z. Xia, M. Leng, Y. Zhou, D.-J. Xue, J. Zhong, L. Gao, H. Song, J. Tang, Synthesis and characterization of hydrazine solution processed $\text{Cu}_{12}\text{Sb}_4\text{S}_{13}$ film, *Sol. Energy Mater. Sol. Cells* 144 (2016) 33-39.
- [75] M. Baláž, E. Dutková, Z. Bujňáková, E. Tóthová, N.G. Kostova, Y. Karakirova, J. Briančin, M. Kaňuchová, Mechanochemistry of copper sulfides: characterization, surface oxidation and photocatalytic activity, *J. Alloys Compd.* 756 (2018) 576-582.
- [76] A. Rossi, D. Atzei, S. Da Pelo, F. Frau, P. Lattanzi, K.E.R. England, D.J. Vaughan, Quantitative X-ray photoelectron spectroscopy study of enargite (Cu_3AsS_4) surface, *Surf. Interface Anal.* 31 (2001) 465-470.

- [77] C. An, Y. Jin, K. Tang, Y. Qian, Selective synthesis and characterization of famatinite nanofibers and tetrahedrite nanoflakes, *J. Mater. Chem.* 13 (2003) 301-303.
- [78] L. Wan, C. Ma, K. Hu, R. Zhou, X. Mao, S. Pan, L.H. Wong, J. Xu, Two-stage evaporated CuSbS_2 thin films for solar cells, *J. Alloys Compd.* 680 (2016) 182-190.
- [79] A. Naumkin, A. Kraut-Vass, NIST X-ray photoelectron spectroscopy database, NIST standard reference database 20, version 4.1, US Secretary of Commerce on behalf of the United States of America, 2012.
- [80] F.-H. Sun, C.-F. Wu, Z. Li, Y. Pan, Asfandiyar, J. Dong, J.-F. Li, Powder metallurgically synthesized $\text{Cu}_{12}\text{Sb}_4\text{S}_{13}$ tetrahedrites: phase transition and high thermoelectricity, *RSC Adv.* 7 (2017) 18909-18916.
- [81] J. Wang, M. Gu, Y. Bao, X. Li, L. Chen, Quick fabrication and thermoelectric properties of $\text{Cu}_{12}\text{Sb}_4\text{S}_{13}$ tetrahedrite, *J. Electron. Mater.* 45 (2016) 2274-2277.
- [82] R. Chetty, A. Bali, M.H. Naik, G. Rogl, P. Rogl, M. Jain, S. Suwas, R.C. Mallik, Thermoelectric properties of Co substituted synthetic tetrahedrite, *Acta Mater.* 100 (2015) 266-274.
- [83] Y. Yan, H. Wu, G. Wang, X. Lu, X. Zhou, High thermoelectric performance balanced by electrical and thermal transport in tetrahedrites $\text{Cu}_{12+x}\text{Sb}_4\text{S}_{12}\text{Se}$, *Energy Storage Mater.* 13 (2018) 127-133.